

Fabrication and characterization of aluminum SQUID transmission lines

Luca Planat,¹ Ekaterina Al-Tavil,¹ Javier Puertas Martínez,¹ Rémy Dassonneville,¹ Farshad Foroughi,¹ Sébastien Léger,¹ Karthik Bharadwaj,¹ Jovian Delaforce,¹ Vladimir Milchakov,¹ Cécile Naud,¹ Olivier Buisson,¹ Wiebke Hasch-Guichard,¹ and Nicolas Roch¹

¹*Univ. Grenoble Alpes, CNRS, Grenoble INP, Institut Néel, 38000 Grenoble, France**

We report on the fabrication and characterization of $50\ \Omega$, flux-tunable, low-loss, SQUID-based transmission lines. The fabrication process relies on the deposition of a thin dielectric layer (few tens of nanometers) via Atomic Layer Deposition (ALD) on top of a SQUID array, the whole structure is covered by a non-superconducting metallic top ground plane. We present experimental results from five different samples. We systematically characterize their microscopic parameters by measuring the propagating phase in these structures. We also investigate losses and discriminate conductor from dielectric losses. This fabrication method offers several advantages. First, the SQUID array fabrication does not rely on a Niobium tri-layer process but on a simpler double angle evaporation technique. Second, ALD provides high quality dielectric leading to low-loss devices. Further, the SQUID array fabrication is based on a standard, all-aluminum process, allowing direct integration with superconducting qubits. Moreover, our devices are *in-situ* flux tunable, allowing mitigation of uncertainty inherent to any fabrication process. Finally, the unit cell being a single SQUID (no extra ground capacitance is needed), it is straightforward to modulate the size of the unit cell periodically, allowing band-engineering. This fabrication process can be directly applied to traveling wave parametric amplifiers.

I. INTRODUCTION

Being able to reproduce the rich physics of non-linear fiber optics [1] in the microwave domain would be a major milestone in microwave physics, since the nonlinearities at stake in this frequency range are orders of magnitude larger than in the optical domain. Non-linear optical fibers have brought fiber amplifiers, a key technology for communication systems but are also very appealing to quantum optics since their dispersion can be tailored to create photonic crystals, allowing the investigation of phenomena such as frequency translation of single photons [2]. In the microwave domain, electrical signals propagate in transmission lines [3]. The quantum nature of these microwave photons can usually be discarded, unless the circuits in which they propagate are cooled down to very low temperatures (below 100 mK). Under these conditions, we speak about circuit Quantum Electrodynamics (cQED) [4]. While in the optical domain non-linearity can be enhanced by doping fibers with rare-earth materials, microwave superconducting quantum circuits can be made strongly non-linear and low-loss by combining superconducting materials and Josephson junctions [5] or by taking advantage of the self-non-linearity of disordered superconductors [6]. This approach has been very successful and lead to the observation of strong light-matter coupling [7], resonance fluorescence with extinction as high as 94% [8] or near quantum-limited parametric amplifiers [9] since it combines both dissipationless and very nonlinear characteristics. However, all these experiments rely on resonant structures – the microwave equivalent of optical cavities.

So far, only few experiments used nonlinear transmission lines – the microwave equivalent of nonlinear optical fibers – in the quantum regime. One notable exception is the demonstration of Traveling Wave Parametric Amplifiers based on either Josephson junctions [10, 11] or disordered superconductors [12–15]. The small number of experimental implementations is explained by the fact that fabricating a long, low-loss, impedance matched, nonlinear transmission line is very demanding. In the case of a Josephson junction transmission line (JJ-TL), nonlinearity is strong [16], sparing the need for long structures. The challenge here is to lower the naturally large impedance of Josephson junction arrays [17] compared to $50\ \Omega$ – by increasing their capacitive effect to the ground, which asks for very concentrated capacitors – while maintaining sufficient low losses. Combining all these requirements was demonstrated using a complex niobium tri-layer fabrication process [18]. Disordered superconductor transmission lines, on the other hand, are mainly limited by their relatively weak nonlinearity. Obtaining sizable nonlinear quantum effects requires meter-long structures, which are strongly prone to fabrication defects [13, 19].

In this work, we present a SQUID transmission line (S-TL) fabricated using a simple, aluminium-based process. Impedance matching is obtained via a top ground plane separated from the SQUID array by a very thin alumina layer. These S-TL show losses on-par with previously reported values [10] and a characteristic impedance close to $50\ \Omega$. This impedance can be adjusted *in-situ*, owing to the flux tunability of the structure [20]. Furthermore, thanks to the simple architecture of our S-TL, the impedance of each unit cell can be tailored at will to create photonic-crystal-like transmission lines [21, 22]. In this article two types of devices, based on the exact same fabrication process, are presented: $50\ \Omega$ matched S-TL and resonant structures made of shorter S-TL. The

* nicolas.roch@neel.cnrs.fr

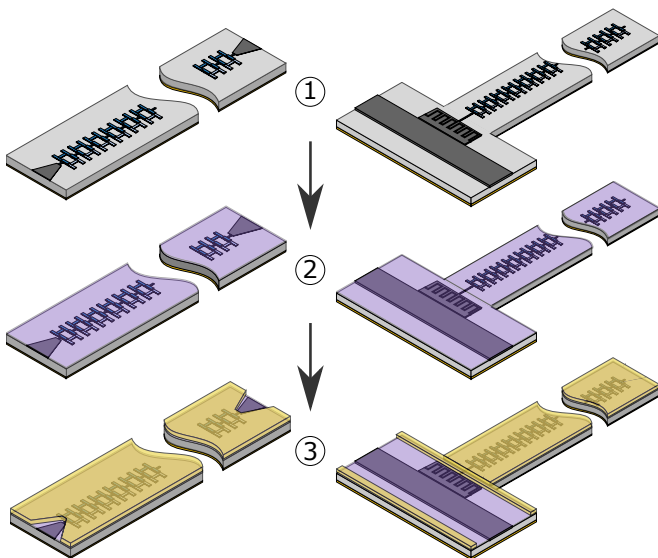


FIG. 1. **Fabrication flow for SQUID-based transmission lines and resonators.** Step 1: fabrication of long SQUID arrays using electron-beam lithography and double angle evaporation of aluminium. Step 2: Deposition of a conformal alumina layer via Atomic Layer Deposition (ALD). Step 3: Evaporation of a thick metallic layer (gold or copper) acting as an electrical ground. This layer is patterned using a combination of electron-beam lithography and lift-off. (Inset:)

latter are used as test structures to characterise our fabrication process in the single microwave photon regime.

This article is organized as follows. In Section II we introduce the fabrication flow and the microwave design of the S-TL. Section III presents the low temperature microwave properties of five different devices. Section IV and Section V focus on the microscopic origins of S-TL losses and their strong power dependence respectively. In the last section magnetic flux response of the S-TL is presented.

II. FABRICATION PROCESS

In this section we detail the fabrication process of SQUID-based transmission lines. Four different batches were obtained using this recipe. Five different devices were then characterized at very low temperatures, as reported in Table I. Devices are fabricated on high-resistivity silicon substrates (thickness 275 μm).

The back side of the silicon wafer is covered by a thin layer of titanium (10 nm, for adhesive purpose) and a thick layer of gold (200 nm) to ensure good thermal and electrical contact to the sample holder. The fabrication process relies on three simple steps summarised in Fig. 1. First a SQUID array is fabricated using double angle evaporation of aluminium (evaporator MEB550S from Plassys), separated by an *in-situ* oxidation to grow the tunnel barrier. For batch 1, 2 and 3, the oxida-

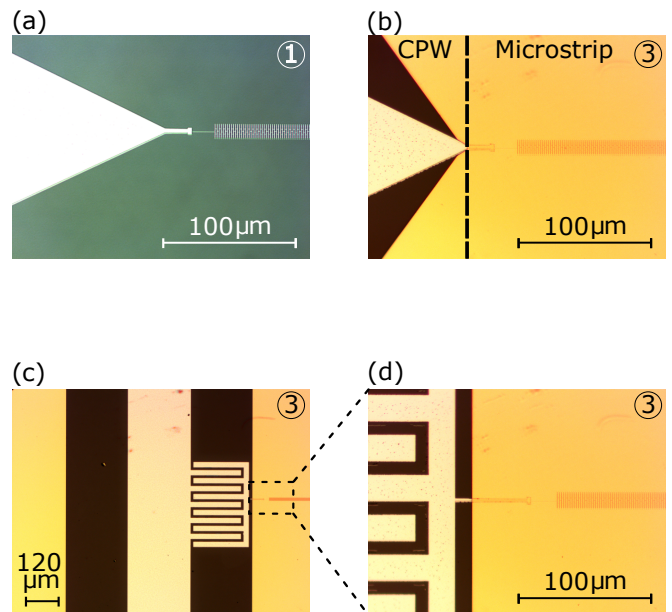


FIG. 2. **Pictures of samples from the first batch.** Pictures a and b display SQUID-based transmission lines whereas c and d are showing details of resonant structures used as control samples. Every picture is labeled by a number corresponding to a fabrication step as shown in Fig. 1. (a) Input of the SQUID-based transmission line after the first step. Left side of the picture: bonding pad with tapered shape. Right side of the picture: few dozens of SQUID. (b) Same structure but after step 3. The gold layer is deposited everywhere but on the bonding pad. SQUID are still distinguishable from below the alumina and gold layers. (c) Picture of the resonant structure after step 3. The feed-line is visible in the middle. On the right side: inter-digital capacitor coupling the feed-line to a section of SQUID-based transmission line (623 unit cells). (d) Zoom in.

tion pressure is 4 torr, for batch 4 it is 1 torr. The resist mask is patterned with a 100 keV electron beam writer (model nB5 from NanoBeam) to allow bridge free fabrication [23]. The typical size of a single Josephson junction is ten microns high and half a micron wide (see Appendix A). A unit cell (two Josephson junctions plus connecting wires in a loop) is about 3 μm wide. This technique allows fabrication of low disorder arrays combining up to 2000 unit cells [24]. However, one of the main difficulty in fabricating such long arrays are stitching errors, coming from a wrong focus of the e-beam due to unavoidable tilt in the substrate. To overcome them, we use the *focus map* feature of our electron beam writer, allowing to readjust dynamically the focus during the writing process. This is achieved by fitting, prior to the writing process, the surface of the chip (8.1 mm \times 8.1 mm) by a tilted plane. The fit is done by measuring the four corners' height where gold marks were previously deposited. The array is terminated by tapered bonding pads (respectively coupling capacitance) as shown in Fig. 2b (resp. d). During step 2, a thin film of alumina is deposited via Atomic Layer Deposition (ALD) using the Savannah

system, from Cambridge Nanotech. The sample is inserted inside a chamber pumped down to 0.29 mbar. We tried two different deposition temperatures, 150 °C and 200 °C, to infer the effect of temperature on the dielectric quality. Thicknesses of the various films are reported in Table I. ALD films combine low microwave losses and conformal deposition. This latter property is crucial to guarantee electrical isolation between the SQUID and the top ground plane deposited during step 3. Access to the bonding pads is guaranteed by windows in this metallic layer. These openings are obtained via a second lithography step and lift-off of the metallic film. We checked that the thickness of the alumina layer is not affected by this subsequent step. Finally, we could easily contact the bonding pads through the alumina layer using micro-bonding given the thickness of this layer (less than 40 nm).

Device	A	B	C	D	E
Batch	1	2	2	3	4
Type	TL	TL	Res	TL	TL
ALD temperature (°C)	150	150	150	200	150
Dielectric thickness (nm)	38	38	38	28	28
Ground thickness (nm)	200	400	400	400	1000
Ground Material	Au	Au	Au	Au	Cu
JJ size H(μm)xW(μm)	12.0 x 0.45	10.5 x 0.40	10.5 x 0.40	12.0 x 0.45	12.0 x 0.45
L_J (pH)	83	125	125	135	51
C_J (fF)	490	380	380	485	485
C_g (fF)	34.0	26.0	31.0	46.0	50.5
Phase velocity (10^6 m.s ⁻¹)	1.96	1.76	1.62	1.32	2.06
$\tan \delta$ (10^{-3})	6.5	6.0	5.0	4.0	6.5
L_c (10^{-4}) (m ⁻¹ .Hz ^{-$\frac{1}{2}$})	2.5	1.0	x	0.8	not measurable
Phase calib. Method	Switch	Switch	N/A	Thru	Thru

TABLE I. Summary of the five samples presented in this article. Four are transmission lines (TL) and one is a resonator (Res). Main fabrication characteristics, SQUID characteristics and loss coefficients are summarized. Calibration methods are also reported

Regarding microwave engineering, we designed the SQUID arrays as a 50Ω microstrip transmission line. Since our SQUID display a typical inductance $L \approx 100$ pH, and a characteristic impedance $Z_c = \sqrt{L/C_g} \approx 50 \Omega$ is being sought, it requires a shunt capacitance $C_g \approx 40$ fF. We model C_g as a planar capacitance $C_g = \epsilon_0 \epsilon_r S/t$ (where ϵ_0 is the vacuum permittivity and S the SQUID's area). Given we are using alumina as the insulator (dielectric constant $\epsilon_r \approx 9.8$) it translates into

a dielectric thickness of $t \approx 30$ nm. These numbers lead to a transmission line with a microstrip geometry with unique features, such as wave velocity below 1% of the light velocity while being matched to 50Ω environment. We also designed a smooth transition from microstrip geometry to Coplanar Waveguide (CPW) geometry to allow for large bonding pads. This transition is shown in Fig. 2.b. We used a conventional tapered shape to keep the impedance constant between the bonding pad and the CPW-microstrip transition. Strictly speaking this is not a CPW geometry since the aluminum layer and the top ground are not exactly in the same plane as they are separated by the alumina layer. Nevertheless, electromagnetic simulations show that the electric field profile is not altered, and that approximating this geometry as a CPW is correct. Indeed alumina and silicon have close dielectric constants and a step of a few tenth of nanometers is negligible compared to the lateral distance between the aluminum and the ground of few hundreds of micron. Regarding resonators, the section of the SQUID-based transmission line (length is approximately 600 unit cells) is capacitively coupled to a feed-line as shown in Fig. 1 and Fig. 2.c and d.

III. CRYOGENIC MICROWAVE PROPERTIES

We now turn to the microwave characterization of these samples at very low temperature ($T = 20$ mK). Measurements were carried out using a standard cryogenic setup. First we measure the dispersion relation (angular frequency versus wave-vector) of the samples. The experimental protocol to access such quantities is not the same for the transmission lines and the resonant structures. The latter is obtained via two-tone spectroscopy [25, 26]. The former follows the procedure explained in [10]. The idea is to measure the propagating phase ϕ of a microwave tone along the device under test (DUT). A proper calibration is needed to remove the contribution of the cryogenic measurement setup. To do so, we used two calibration techniques. For samples A and B, a cryogenic microwave switch (model R577433000 from Radiall) would shunt the sample at 20 mK to infer, during the same cooldown, both the contribution of the setup and of the DUT. For samples D and E we used a simple thru to calibrate the contribution of the setup. We placed a thru in CPW geometry instead of the actual chip containing the SQUID-based transmission line. This technique requires two different cool-downs but gives a better estimate of the setup contribution (wire bonds are similar to the DUT and there are no extra cables connecting to the switch to the DUT). The last calibration step is to ensure that at zero frequency, this propagating phase is zero. Indeed the phase measured with a Vector Network Analyser (VNA) is defined modulo 2π . We use a procedure similar to Macklin et al. [10] to adjust it properly. The propagating phase ϕ can then be linked to

the wave-vector k using:

$$k(\omega) = \frac{\phi(\omega)}{L}, \quad (1)$$

where L is the length of the SQUID array and is perfectly known since both the unit cell size a and the total number of unit cells N_J are well known. Two measured dispersion relations are plotted in Fig. 3. Grey points in Fig. 3.a were discarded from the fitting procedure since they are out of the operating frequency range (3 GHz to 14 GHz) of our cryogenic HEMT amplifier (model LNF-LNC1-12A from Low Noise Factory).

To infer the microscopic parameters of the samples L_J and C_g (see Appendix A), we fitted their dispersion relations using the following model [26]

$$\omega_k = \omega_{\text{plasma}} \left(\sqrt{\frac{1 - \cos ka}{1 - \cos ka + C_g/2C_J}} \right), \quad (2)$$

where the Josephson capacitance C_J is a fixed parameter and taken as 45 fF per micro meter square [27] and ω_{plasma} is the plasma frequency of a SQUID and reads $\omega_{\text{plasma}} = 1/\sqrt{L_J C_J}$.

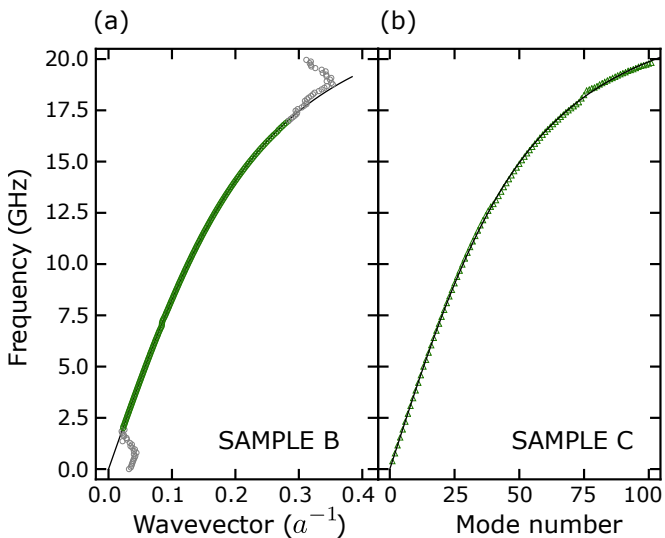


FIG. 3. **Dispersion relations** (a) Dispersion relation of a SQUID-based transmission line (sample B). Black line is a fit of the experimental data to Eq. (2). (b) Dispersion relation of a resonant structure (sample C). Data were acquired via two tone spectroscopy and fitted using Eq. (2) as well.

The values found for C_g throughout the different batches follow the correct trend: the bigger the junctions are, the bigger C_g is; the thinner the dielectric is, the bigger C_g is. Regarding L_J , we experienced a drift from batch 1 to batch 3 towards larger inductance. Junctions from batch 4 were oxidized with a pressure of 1 torr instead of 4 torr in order to compensate this drift. Also, sample B and C should display the same microscopic parameters since they were fabricated within the same batch (see Table I). The size of sample B unit cells was

modulated periodically while sample C has uniform cells. This modulation is very small (6% amplitude) and only opens a small photonic gap over a band of few hundreds of megahertz in the dispersion relation. This does not affect its overall shape as shown in Fig. 2, where only a small kink can be seen around 7 GHz. We find the same values for the Josephson inductance but there is a small discrepancy in the ground capacitance which might be due to the fitting procedure or to uniformity in the dielectric layer. Finally, we can define a low frequency ($\omega \ll \omega_{\text{plasma}}$) characteristic impedance $Z_c = \sqrt{L_J/C_g}$ for both samples, leading to Z_c between 65 Ω and 70 Ω .

IV. CONDUCTOR AND DIELECTRIC LOSSES

Losses of the transmission line is another very important parameter. To understand loss mechanisms we probed the calibrated transmission of S-TL, using the calibration technique presented in the previous section. Fig. 4 shows this calibrated transmissions for samples A, B, D and E. They show losses on the order of 5 dB/cm at 6 GHz. Although these losses are significant, they are comparable to previously reported structure based on Josephson junctions [10]. A more thorough study can explain the different loss mechanisms of our devices. Seen as microstrip lines, our samples suffer from two well known phenomena in microwave engineering: dielectric and conductor losses [28]. Within the superconducting community, the latter form of losses have been rightfully neglected since there are no significant losses inside the superconductors nor in thick metallic grounds (superconducting or not). Such assumptions are not valid anymore in our geometry. Although the central conductor is superconducting, the top ground plane is made of a non superconducting metal (gold or copper, for the last version), with a finite thickness (hundreds of nanometers), comparable to the skin depth. This configuration can lead to non negligible conductor losses as we will see later. To determine the origin of losses, we fit the calibrated transmission of the S-TL with a simple model [3], where α_c and α_d represent the conductor and dielectric losses respectively. The total attenuation of the line can then be expressed as

$$A = e^{(\alpha_c + \alpha_d)L}, \quad (3)$$

Considering our microstrip geometry with very large shunt capacitance, it is safe to assume that the electrical field is mainly confined within the top alumina substrate. Thus, we model the dielectric loss as α_d as [3]:

$$\alpha_d = \frac{k \tan \delta}{2} \quad (4)$$

We thus have a direct relation between the angular frequency ω_k of the signal and the dielectric loss through a free parameter $\tan \delta$. In microwave engineering, it is defined as the ratio of the imaginary part over the real part of the complex permittivity of the medium.

Regarding α_c , as mentioned before, we will only take into account top ground loss.

Given the microstrip line geometry of our system, we consider [29]:

$$\alpha_c = \frac{R}{Z_0}, \quad (5)$$

where Z_0 is the characteristic impedance of the line, and R is the *radio resistance* per unit length. R is given by

$$R = \frac{R_s}{\mu_0} \frac{\delta l}{\delta n}, \quad (6)$$

where $R_s = \sqrt{\omega\mu_0/2\sigma}$ is the skin resistance of the conductor, μ_0 the vacuum permeability and the ratio $\delta l/\delta n$ characterises the change of inductance per unit length δl when the conductor walls recede by a distance δn . In a metal the current flows within the skin depth $\delta_s = \sqrt{2/\omega\mu_0\sigma}$. If the conductor is much thicker than δ_s , the change of inductance is negligible. This amounts to considering the ratio $L\delta l/\mu_0\delta n$ in the order of unity.

On the other hand if the conductor thickness is comparable or smaller than δ_s , then the change of δl is large, the ratio is much larger than one and conductor loss increases. Obtaining a quantitative value of $L\delta l/\mu_0\delta n$ requires 3D electromagnetic simulations. It is beyond the scope of this paper. However this formula gives the correct order of magnitude for α_c when the top ground plane is thicker than δ_s .

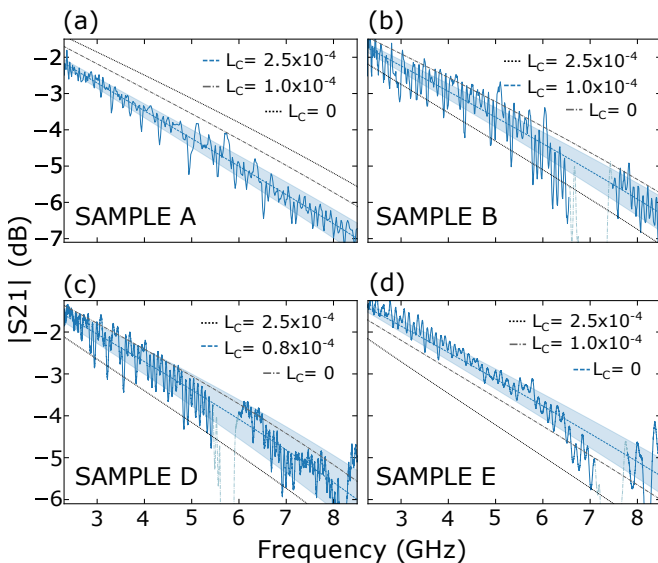


FIG. 4. **Calibrated, low temperature transmission of S-TL.** Solid (dashed) lines are experimental data (fits to Eq. (3)). Values of fitting parameters are reported in Table I. Shaded blue areas represent $5 \cdot 10^{-4}$ uncertainty on $\tan \delta$. Black dotted and grey dash-dotted lines are obtained using Eq. (3) with the same $\tan \delta$ but with different conductor loss (values indicated in each panel in $\text{m}^{-1}\text{Hz}^{-\frac{1}{2}}$). All data were taken with input power $P_{\text{in}} = -106 \text{ dBm} \pm 3 \text{ dBm}$ except for sample A where $P_{\text{in}} = -101 \text{ dBm} \pm 3 \text{ dBm}$.

Another important feature is that α_c should scale as the square root of the frequency. Then we model α_c as

$$\alpha_c = L_c \sqrt{f}, \quad (7)$$

where f is the signal frequency and L_c is a prefactor accounting for the conductor losses, which should decrease as the thickness of the top ground metal increases. Then we fit the attenuation of the various S-TL characterized in this work using two parameters: $\tan \delta$ and L_c . Although S-TL attenuation shows a monotonous trend versus frequency (see Fig. 4), we managed to fit independently these two parameters. Indeed surface resistivity depends on the square root of the signal frequency and dielectric loss varies linearly with frequency. In other words, dielectric loss sets the slope of the insertion loss at high frequencies, while conductor loss affects the lower frequencies. All the obtained fitting parameters are presented in Table I.

We now turn to the discussion of these parameters. First we measured that $\tan \delta$ remains between $6.5 \cdot 10^{-3} \pm 5 \cdot 10^{-4}$ and $4 \cdot 10^{-3} \pm 5 \cdot 10^{-4}$ for low-power measurements, which is on par with previously demonstrated JJ-TL [10]. Table I summarises the different deposition parameters of alumina. We observe that a higher deposition temperature seems to improve dielectric loss. However, given the uncertainty over the loss tangent in this study, we do not claim that deposition temperature is the most important parameters to reduce dielectric loss. However, such values of loss tangent are very promising, since already comparable to state-of-the-art. Moreover, loss tangents as low as $2.45 \cdot 10^{-3}$, in the single photon regime, was reported for alumina with similar thickness, at very low temperatures [30].

Regarding conductor loss, we observe that as the top-ground thickness increases, L_c drops. We have plotted for what we consider to be the best conductors loss (in dashed blue) for each version as well as other values of conductors (in dashed grey) loss to give insights on the confidence interval (see Fig. 4). As a reminder, batch 2 and 3 should have the same conductor loss since their top-ground thickness is the same. Another interesting point is that a gold conductivity of 100 MS m^{-1} was reported at very low temperature [31]. This translates into a skin depth $\delta_s = 600 \text{ nm}$ at 7 GHz . We can expect the same order for copper ground as gold and copper have close conductivity at room temperature. Batch 1, where the top-ground thickness was well below δ_s , shows strong conductor loss. In the other batches, with thicker ground planes, losses decreased. Until batch 4 (thickness $1 \mu\text{m}$) where conductor loss is below what we can measure [32].

V. POWER-DEPENDENT LOSSES

We now report on the power-dependence of these losses. In both the matched transmission lines and the

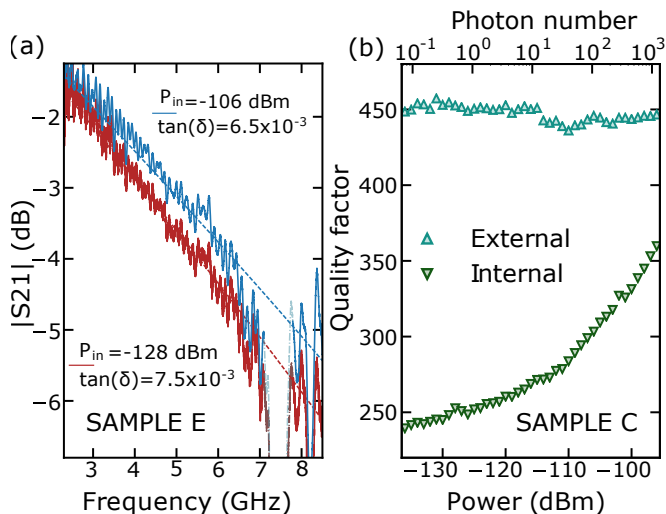


FIG. 5. **Power dependence of losses.** For both panels, power is referred to the input of the device. (a) S-TL calibrated transmission (sample E). Input power and fitted loss tangent are reported directly on the figure. (b) Quality factors (internal and external) of a given resonant mode of sample C (angular frequency $\omega_0 = 2\pi \times 7.47$ GHz). Fit is obtained for the same resonance at various input powers (see Appendix B). Photon number (top axis) is obtained using Eq. (B2).

resonant structures we observe that losses decrease when power increases (Fig. 5). The fitted loss tangent of the S-TL presented in Fig. 5.a depends on input power and saturates at low power, close to $\tan \delta = 7.5 \times 10^{-3} \pm 5 \times 10^{-4}$. Fitted external and internal quality factors of a given resonant mode are plotted in Fig. 5b for various input powers in the feedline. The external quality factor remains constant while the internal quality factors increases with input power. This observation is in agreement with what was reported in a JJ-TL [10]. At very low powers, close to the single photon regime, losses saturate. This is consistent with the presence of Two-Level-Systems within the dielectric layer [30]. The internal quality factor and loss tangent are linked via $Q_i = 1/\tan \delta$ [3]. We can compare quality factors from sample C, which is from the same batch as sample B (calibrated transmission is shown in Fig. 4.b). For sample B, at low signal power, close to the loss tangent saturation, we find $\tan \delta = 6.0 \times 10^{-3} \pm 5 \times 10^{-4}$. We compare this value to low power quality factors measured for sample C. At $P_{\text{input}} = -136$ dBm [33] ($\bar{n} \approx 0.1$) we find, depending on the resonant mode, an internal quality factor between $Q_{i,\text{min}} = 125$ and $Q_{i,\text{max}} = 300$, with a mean value around 200 (see Appendix C). This translates into a loss tangent of $\tan \delta_{\text{mean}} = 1/200 = 5.0 \times 10^{-3}$, in good agreement with the loss tangent found for sample B.

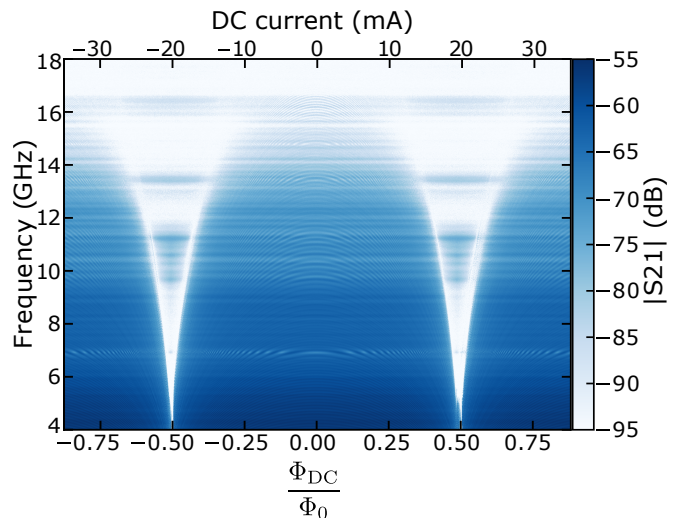


FIG. 6. **Transmission of a S-TL versus flux and frequency (sample E).**

VI. FLUX MODULATION

Finally, we describe the flux tunability of a S-TL. Fig. 6 shows the flux dependence of the transmission of sample E. At low frequencies, below 8 GHz, the transmission is mostly flat with no visible ripples. At higher frequencies one can observe flux-dependent standing waves. This is explained by spurious reflections between the S-TL and its microwave environment. These reflections could be caused by wire-bonds or a non-optimized PCB-to-connector transition. We emphasize the smooth behavior of the device during flux tuning, despite the large number of SQUID. This stability can be attributed to our choice of having a non-superconducting ground plane on top of the SQUID, which prevents flux trapping and effects due to Meissner currents. Interestingly the plasma frequency of the SQUID can be directly observed as a drop in transmission. At zero flux it is above 20 GHz but drops almost down to zero for magnetic fluxes close to half a fluxoid.

VII. CONCLUSION

We have introduced a process to fabricate SQUID transmission lines. It is simple, low-loss and offers in-situ flux tunability. The impedance matching to 50 Ω relies on a simple yet effective idea: a metallic electrical ground deposited on top of the SQUID array, which are separated by a thin alumina layer, guaranteeing electrical isolation. Impedance matching was demonstrated at very low temperatures (20 mK) and very low power (single photon regime). Two loss sources were identified; conductor losses due to the finite thickness of the metallic ground compared to the skin depth and dielectric losses consistent with the presence of two-level systems. We

showed that increasing the thickness of the ground plan improves conductor losses. Regarding dielectric losses, we measured loss tangent down to 5.0×10^{-3} . This value is comparable to what was reported in the literature [10] but could be improved given the values previously obtained for alumina [30]. Finally, we demonstrated *in-situ* flux tunability of these S-TL. These devices could be used as Josephson Traveling Wave Parametric Amplifiers, based on four-wave mixing [10, 11, 22]. Their flux-tunability offers interesting perspectives regarding three-wave mixing [34, 35] or Kerr-free [36, 37] J-TWPA. These devices could also be used to perform new quantum optics experiments in the microwave domain [38].

ACKNOWLEDGMENTS

Very fruitful discussions with D. Basko, K. R. Amin, and A. Ranavive are acknowledged. We also thank M. Selvanayagam for critical reading of the manuscript. The samples were fabricated in the Nanofab clean room. This research was supported by the ANR under contracts CLOUD (project number ANR-16-CE24-0005) and the European Union's Horizon 2020 Research and Innovation Programme, under grant agreement No. 824109, the European Microkelvin Platform (EMP). J.P.M. acknowledges support from the Laboratoire d'excellence LANEF in Grenoble (ANR-10-LABX-51-01). R.D. and S.L. acknowledge support from the CFM foundation and the 'Investissements d'avenir' (ANR-15-IDEX-02) programs of the French National Research Agency.

Appendix A: Electrical models

In this section, we present the electrical models used to describe the samples we measured. For the S-TL, we used a standard telegrapher model where one SQUID is a cell composed of a nonlinear Josephson inductance L_J , a ground capacitance C_g and a Josephson capacitance C_J . The electrical sketch is shown in Fig. 7.a. The SQUID array is connected to 50Ω pads via wire bonding. For the SQUID-based resonator, we use the same model. The only difference is that the line is capacitively coupled to the 50Ω feedline. An electrical sketch is drawn in Fig. 7.b.

Appendix B: S-Res measurements

We present here low temperature measurements of sample C. It is 600 SQUID long with a free spectral range of 350 MHz. Transmission close to resonance is fitted using the formula [39]:

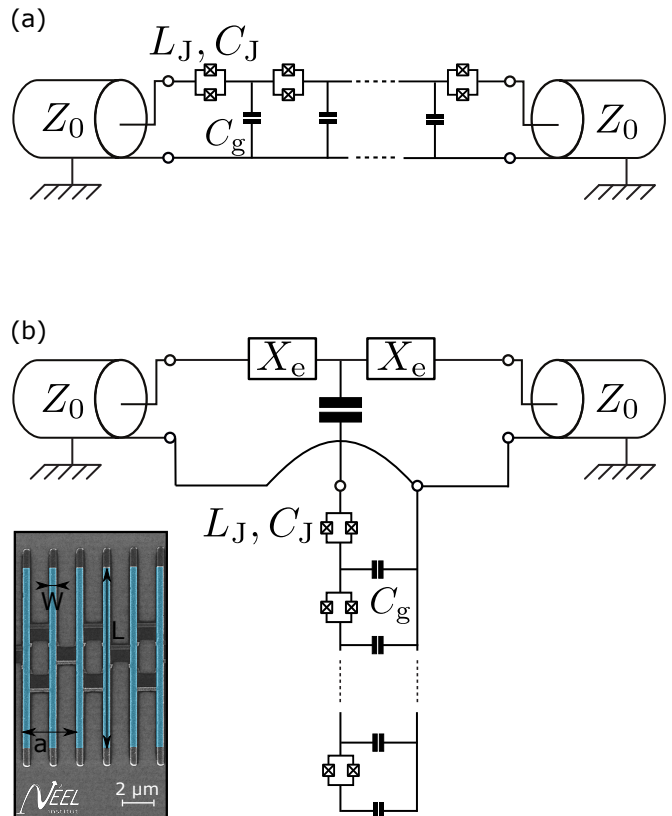


FIG. 7. Electrical sketches of the two measured structures. (a) Electrical model of the S-TL. (b) Electrical model of the S-Res. **Inset** SEM picture of 3 SQUID. Highlighted blue regions are Josephson junctions.

$$S_{21} = \frac{Z_0}{Z_0 + iX_e} \frac{1 + 2iQ_i(\frac{\omega - \omega_0}{\omega_0})}{1 + \frac{Q_i}{Q_e Z_0(Z_0 + iX_e)} + 2iQ_i(\frac{\omega - \omega_0}{\omega_0})}, \quad (\text{B1})$$

where Z_0 is the feedline characteristic impedance, X_e the reactance from the bonding wires, ω_0 the resonance frequency of the resonator, Q_i and Q_e the internal and external quality factors, respectively. In Fig. 8 we present 5 resonances from 6.00 GHz to 7.75 GHz (amplitude and phase) from the S-Res at very low input power. Black lines are fits to Eq. (B1). From this equation we extract internal and external quality factors (see Fig. 5.b) that we plot as a function of input power and photon number inside the cavity. The photon number was calibrated using input/output theory [39]:

$$\bar{n} = \frac{2 \frac{\omega_0}{Q_e}}{\hbar \omega_0 (\frac{\omega_0}{Q_e} + \frac{\omega_0}{Q_i})^2} P_{\text{input}} \quad (\text{B2})$$

where ω_0 is the resonant frequency of the cavity and P_{input} the signal input power.

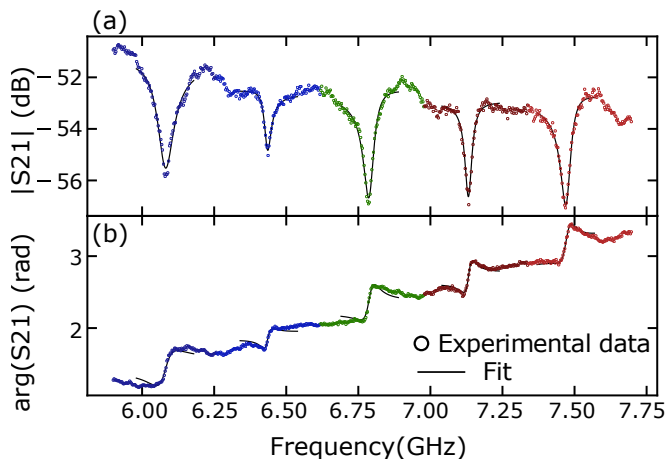


FIG. 8. Transmission $|S_{21}|$ of the hanger resonators fitted close to the resonances

Appendix C: Frequency dependency of the internal quality factor

In this section, we present extracted quality factors for very low input power, $P_{\text{input}} = -136\text{dBm} \pm 3\text{dBm}$, that translates into 0.1 photon (see Appendix B for the photon number calibration). At very low photon number,

close to the saturation of the losses, we observe a internal quality factor of 200 with a spread between 125 and 300 for different resonant frequencies as shown in Fig. 9.

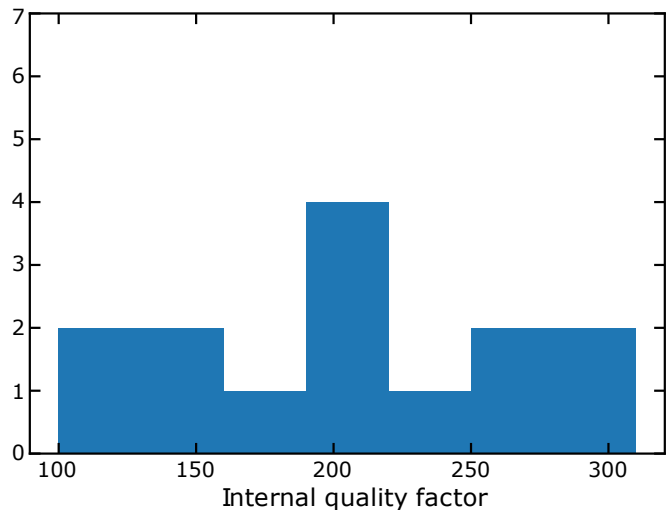


FIG. 9. Internal quality factors extracted from the fit of 14 modes in sample C between 3.86 GHz and 8.46 GHz at an input power $P_{\text{in}} = -136\text{dBm} \pm 3\text{dBm}$, corresponding to the single photons level. We observe a spread of the internal quality factor around 200 at this power.

-
- [1] G. Agrawal, *Nonlinear fiber optics; 5th ed.*, Optics and Photonics (Elsevier, Burlington, MA, 2012).
 - [2] H. J. McGuinness, M. G. Raymer, C. J. McKinstrie, and S. Radic, Quantum Frequency Translation of Single-Photon States in a Photonic Crystal Fiber, *Physical Review Letters* **105**, 093604 (2010).
 - [3] D. M. Pozar, *Microwave engineering* (John Wiley & Sons, 2009).
 - [4] R. J. Schoelkopf and S. M. Girvin, Wiring up quantum systems, *Nature* **451**, 664 (2008).
 - [5] M. H. Devoret, Quantum fluctuations in electrical circuits, *Les Houches* (1995).
 - [6] C. C. Chin, D. E. Oates, G. Dresselhaus, and M. S. Dresselhaus, Nonlinear electrodynamics of superconducting NbN and Nb thin films at microwave frequencies, *Phys Rev B* **45**, 4788 (1992).
 - [7] A. Wallraff, D. I. Schuster, A. Blais, L. Frunzio, R.-S. Huang, J. Majer, S. Kumar, S. M. Girvin, and R. J. Schoelkopf, Strong coupling of a single photon to a superconducting qubit using circuit quantum electrodynamics, *Nature* **431**, 162 (2004).
 - [8] O. Astafiev, A. M. Zagoskin, A. A. Abdumalikov, Y. A. Pashkin, T. Yamamoto, K. Inomata, Y. Nakamura, and J. S. Tsai, Resonance Fluorescence of a Single Artificial Atom, *Science* **327**, 840 (2010).
 - [9] M. A. Castellanos-Beltran, K. D. Irwin, G. C. Hilton, L. R. Vale, and K. W. Lehnert, Amplification and squeezing of quantum noise with a tunable Josephson metamaterial, *Nature Physics* **4**, 928 (2008).
 - [10] C. Macklin, K. O'Brien, D. Hover, M. Schwartz, V. Bolkhovskiy, X. Zhang, W. Oliver, and I. Siddiqi, A near-quantum-limited josephson traveling-wave parametric amplifier, *Science* **350**, 307 (2015).
 - [11] T. White, J. Mutus, I.-C. Hoi, R. Barends, B. Campbell, Y. Chen, Z. Chen, B. Chiaro, A. Dunsworth, E. Jeffrey, *et al.*, Traveling wave parametric amplifier with josephson junctions using minimal resonator phase matching, *Applied Physics Letters* **106**, 242601 (2015).
 - [12] B. H. Eom, P. K. Day, H. G. Leduc, and J. Zmuidzinas, A wideband, low-noise superconducting amplifier with high dynamic range, *Nature Physics* **8**, 623 (2012).
 - [13] C. Bockstiegel, J. Gao, M. R. Vissers, M. Sandberg, S. Chaudhuri, A. Sanders, L. R. Vale, K. D. Irwin, and D. P. Pappas, Development of a Broadband NbTiN Traveling Wave Parametric Amplifier for MKID Readout, *Journal of Low Temperature Physics* **176**, 476 (2014).
 - [14] M. R. Vissers, R. P. Erickson, H. S. Ku, L. Vale, X. Wu, G. C. Hilton, and D. P. Pappas, Low-noise kinetic inductance traveling-wave amplifier using three-wave mixing, *Applied Physics Letters* **108**, 012601 (2016).
 - [15] S. Chaudhuri, D. Li, K. D. Irwin, C. Bockstiegel, J. Hubmayr, J. N. Ullom, M. R. Vissers, and J. Gao, Broadband parametric amplifiers based on nonlinear kinetic inductance artificial transmission lines, *Applied Physics Letters* **110**, 152601 (2017).
 - [16] Y. Krupko, V. D. Nguyen, T. Weissl, E. Dumur, J. Puer-tas, R. Dassonneville, C. Naud, F. W. J. Hekking, D. M. Basko, O. Buisson, N. Roch, and W. Hasch-Guichard,

- Kerr nonlinearity in a superconducting Josephson metamaterial, *Phys Rev B* **98**, 094516 (2018).
- [17] L. Planat, R. Dassonneville, J. Puertas Martinez, F. Foroughi, O. Buisson, W. Hasch-Guichard, C. Naud, R. Vijay, K. Murch, and N. Roch, Understanding the Saturation Power of Josephson Parametric Amplifiers Made from SQUID Arrays, *Physical Review Applied* **11**, 034014 (2019).
- [18] S. K. Tolpygo, V. Bolkhovskiy, T. J. Weir, L. M. Johnson, M. A. Gouker, and W. D. Oliver, Fabrication process and properties of fully-planarized deep-submicron nb/al–AlO_x/Nb Josephson junctions for vlsi circuits, *IEEE Transactions on Applied Superconductivity* **25**, 1 (2015).
- [19] A. A. Adamyan, S. E. de Graaf, S. E. Kubatkin, and A. V. Danilov, Superconducting microwave parametric amplifier based on a quasi-fractal slow propagation line, *Journal of Applied Physics* **119**, 083901 (2016).
- [20] P. Jung, S. Butz, S. V. Shitov, and A. V. Ustinov, Low-loss tunable metamaterials using superconducting circuits with Josephson junctions, *Applied Physics Letters* **102**, 062601 (2013).
- [21] C. Hutter, E. A. Tholen, K. Stannigel, J. Lidmar, and D. B. Haviland, Josephson junction transmission lines as tunable artificial crystals, *Physical Review B* **83**, 014511 (2011).
- [22] L. Planat, A photonic crystal Josephson traveling wave parametric amplifier, Submitted (2019).
- [23] F. Lecocq, I. M. Pop, Z. Peng, I. Matei, T. Crozes, T. Fournier, C. Naud, W. Guichard, and O. Buisson, Junction fabrication by shadow evaporation without a suspended bridge, *Nanotechnology* **22**, 315302 (2011).
- [24] J. Puertas Martinez, S. Leger, N. Gheeraert, R. Dassonneville, L. Planat, F. Foroughi, Y. Krupko, O. Buisson, C. Naud, W. Hasch-Guichard, S. Florens, I. Snyman, and N. Roch, A tunable Josephson platform to explore many-body quantum optics in circuit-QED, *npj Quantum Information* **5**, 1829 (2019).
- [25] N. Masluk, I. Pop, A. Kamal, Z. Mineev, and M. Devoret, Microwave Characterization of Josephson Junction Arrays: Implementing a Low Loss Superinductance, *Physical Review Letters* **109**, 137002 (2012).
- [26] T. Weissl, B. Küng, E. Dumur, A. K. Feofanov, I. Matei, C. Naud, O. Buisson, F. W. J. Hekking, and W. Guichard, Kerr coefficients of plasma resonances in Josephson junction chains, *Physical Review B* **92**, 104508 (2015).
- [27] A. Fay, *Couplage variable entre un qubit de charge et un qubit de phase*, Ph.D. thesis, Université Joseph-Fourier - Grenoble I (2008).
- [28] K. Gupta, R. Garg, I. Bahl, and P. Bhartia, *Microstrip Lines and Slotlines*, Artech House microwave library (Artech House, 1979).
- [29] M. V. Schneider, Microstrip lines formicrowave integrated circuits, *Bell System Technical Journal* **48**, 1421 (1968).
- [30] C. Deng, M. Otto, and A. Lupascu, Characterization of low-temperature microwave loss of thin aluminum oxide formed by plasma oxidation, *Applied Physics Letters* **104**, 043506 (2014).
- [31] H. Hegger, B. Huckestein, K. Hecker, M. Janssen, A. Freimuth, G. Reckziegel, and R. Tuzinski, Fractal conductance fluctuations in gold nanowires, *Phys. Rev. Lett.* **77**, 3885 (1996).
- [32] If we consider the ratio $L\delta l/\mu_0\delta n$ on the order of unity, the conductor losses $L_c = \frac{\delta l}{\mu_0\delta n} \frac{\sqrt{\mu_0}}{Z_0\sqrt{2\sigma}}$ reads as $L_c = \frac{\sqrt{\mu_0}}{LZ_0\sqrt{2\sigma}}$. By taking $Z_0 = 50\Omega$, $\sigma = 100\text{MSm}^{-1}$ and $L = 7\text{mm}$, we obtain $L_c = 5.5 \times 10^{-7}\text{m}^{-1}\text{Hz}^{-\frac{1}{2}}$. This justifies our choice to set $L_c = 0$ when fitting sample E.
- [33] We estimate the total setup attenuation being $76\text{dB} \pm 3\text{dB}$ as the sum of discrete attenuators (69dB), cable attenuation (5dB) and filter (2dB).
- [34] A. B. Zorin, M. Khabipov, J. Dietel, and R. Dolata, Traveling-wave parametric amplifier based on three-wave mixing in a Josephson metamaterial, 2017 16th International Superconductive Electronics Conference (ISEC) , 1 (2017).
- [35] A. B. Zorin, Josephson traveling-wave parametric amplifier with three-wave mixing, *Phys. Rev. Applied* **6**, 034006 (2016).
- [36] M. T. Bell and A. Samolov, Traveling-wave parametric amplifier based on a chain of coupled asymmetric squids, *Phys. Rev. Applied* **4**, 024014 (2015).
- [37] W. Zhang, W. Huang, M. E. Gershenson, and M. T. Bell, Josephson metamaterial with a widely tunable positive or negative Kerr constant, *Phys. Rev. Applied* **8**, 051001 (2017).
- [38] A. L. Grimsmo and A. Blais, Squeezing and quantum state engineering with Josephson travelling wave amplifiers, *npj Quantum Information* **3**, 20 (2017).
- [39] E. Dumur, *A V-shape superconducting artificial atom for circuit quantum electrodynamics*, Ph.D. thesis, University Grenoble Alpes (2015).